Peng, L.; Jurca, B.; Primo Arnau, AM.; Gordillo, A.; Parvulescu, VI.; García Gómez, H. (2021). Co-Fe Clusters Supported on N-Doped Graphitic Carbon as Highly Selective Catalysts for Reverse Water Gas Shift Reaction. ACS Sustainable Chemistry & Engineering. 9(28):9264-9272. https://doi.org/10.1021/acssuschemeng.1c01401

Co-Fe Clusters Supported on N-Doped Graphitic Carbon as Highly-Selective Catalysts for Reverse Water Gas Shift

Lu Peng,[a, ‡] *Bogdan Jurca,*[b, ‡] *Ana Primo,*[a] *Alvaro Gordillo,*[c] *Vasile I. Parvulescu**[b] *and Hermenegildo García**[a]

[a] Instituto Universitario de Tecnología Química, Universitat Politècnica de València-Consejo Superior de Investigaciones Científicas, Universitat Politècnica de València, Av. De los Naranjos s/n, 46022 Valencia, Spain. E-mail: hgarcia@upv.es (H.G.)

[b] Department of Organic Chemistry and Biochemistry and catalysis, Faculty of Chemistry, University of Bucharest, Bdul Regina Elisabeta 4-12, Bucharest 030016, Romania. E-mail: vasile.parvulescu@chimie.unibuc.ro (V.P.)

[c] BASF SE, 67056 Ludwigshafen am Rhein, Germany.

‡ Both are first authors.

ABSTRACT

Graphitic carbons are suitable supports of metal nanoparticles with catalytic activity. In the present study a procedure starting from biomass waste for the preparation of N-doped graphitic carbon supporting clusters of Fe-Co alloys is reported. These subnanometric Co-Fe clusters supported on N-doped graphitic carbon at metal loading below 0.2 wt.% exhibit high activity for the selective hydrogenation of CO_2 to CO. Operating at 500 ^oC and 10 bars with a H_2/CO_2 molar ratio of 7 and a space velocity of 600 h^{-1}, a conversion of 56 % with a selectivity to CO over 98 % and remarkable stability over 30 h operation was obtained. Interestingly, analogous catalysts based on N-doped graphitic carbon with much higher Co-Fe loadings and average particle size range of 1-5 nm exhibit only half of this activity, with similar CO selectivity. This contrasting behavior reveals the dramatic effect of the particle size in the catalytic activity. In comparison, SiO_2 as support under similar conditions affords CH_4 as the main product.

KEYWORDS Heterogeneous catalysis; CO_2 utilization; Reverse water Gas Shift; Graphene as support; Selective Co-Fe alloy nanoparticles.

INTRODUCTION

There is an urgent need to decrease atmospheric CO_2 emissions in order to mitigate global warming and climate change.[1-3] One possibility to diminish emissions is to implement large-scale CO_2 capture utilizing CO_2 as feedstock for fuels and chemicals.[4-6] CO_2 hydrogenation reaction has attracted considerable attention since it gives access to a wide variety of products of significant industrial interest.[7-11] In this context, one attractive process would be the selective hydrogenation of CO_2 into CO via reverse water gas shift (RWGS).[12-16] Decarbonized syngas in which the CO_2

footprint is negative for CO and zero for H_2 can provide in large-scale fuels and chemicals through existing mature Fischer-Tropsch technology.[17-19] The current challenge is to develop even more active, selective and stable RWGS catalysts based on first raw transition metals.

Numerous transition metal catalysts, including Fe, Co and Ni, have been reported to catalyze CO_2 hydrogenation, but many of them afford less valuable methane (Sabatier reaction) or undergo fast deactivation, particularly when CO is the product.[20, 21] In this context, there exists much current interest in the catalytic activity of single atoms and small clusters of nanometric dimensions (CLs) supported on graphenes or graphitic carbons.[22-25] Doped graphene as support can stabilize metal CLs through strong metal-support interactions, rendering materials that are among those exhibiting the highest catalytic activity.[26] In these precedents, doping, carbon vacancies and graphene lattice defects are proposed to play a crucial role in the stability of the adsorbed metal CLs.[27-31] It could be that the stabilization provided by N-doped, defective graphene could serve to avoid agglomeration of highly unstable small metal CLs, maintaining catalyst activity and selectivity for longer time. Related to the present work, it has been recently reported that N-doped graphene exhibits activity as metal-free catalyst for CO_2 hydrogenation, but methane was the final product.[32]

Continuing with this line of research, it would be of interest to determine the catalytic activity of CLs of Co, Fe and their alloys supported on defective N-doped graphitic carbon for CO_2 hydrogenation. It would be important to determine the activity and stability of these N-doped graphitic carbon supported Fe-Co CLs as a function of their Fe/Co ratio in comparison with analogous Fe-Co catalysts having larger particles trying to find more active, selective and stable catalysts for the RWGS. The present study shows that N-doped graphitic carbon [(N)G] obtained from biomass wastes provides the opportunity to prepare CLs and small nanoparticles (NPs) of single Co and Fe metals and their alloys. Catalytic data show that Fe-Co CLs supported on (N)G

exhibit a remarkable RWGS selectivity and significantly higher activity than analogous catalysts of 1-5 nm particle size. The catalytic behavior of these Fe-Co CLs on (N)G contrasts with the performance of analogous Fe-Co NPs on SiO_2 as support, on which a notably different selectivity towards methane is observed.

EXPERIMENTAL SECTION

Synthesis of Co@(N)G, Fe@(N)G, Co-Fe@(N)G, Co-Fe@G and Co-Fe@SiO_2. Commercially available reagents were purchased from Aldrich and used without further purification.

Preparation of samples 1-10. Samples **1-10** were prepared by impregnation of chitosan beads in 50 vol % aqueous ethanol with iron and cobalt acetates. Briefly, 400 mg chitosan and 250 μL acetic acid were added into 20 mL milli-Q water. After chitosan powder dissolved completely, the solution was introduced dropwise, with a syringe (0.8 mm diameter needle), in an aqueous solution of sodium hydroxide (2 M). The gel microspheres were formed and immersed in NaOH solution for 2 h, then profusely washed with distilled water until the washing water had pH=7. Then, the resulting hydrogel microspheres were washed by a series of ethanol/water baths with an increasing concentration of ethanol (10, 30, 50 vol %, respectively) for 15 minutes in each and immersed in 40 mL (50 vol % aqueous ethanol solution) with different concentration of $Co(OAc)_2$/$Fe(OAc)_2$ for 2 days under slow stirring. After that, the microspheres were dehydrated by suspending them in a series of ethanol/water baths with increasing ethanol concentration (70, 90 and 100 vol %, respectively) for 15 min each and finally dried by supercritical CO_2. The resulting aerogel

microspheres were pyrolyzed under Ar flow (200 mL/min), increasing the temperature at a rate of 2 ^{o}C/min up to 200 ^{o}C for 2 h and then to 900 ^{o}C for 2 h.

Sample **11** was prepared analogously, but starting from introducing alginic solution with metal salts dropwise, with a syringe (0.8 mm diameter needle), in an aqueous solution of $CaCl_2$. The gel microspheres were formed and immersed in metal salt solution for 2 h, then washed by a series of ethanol/water baths with an increasing concentration of ethanol (10, 30, 50, 70, 90 and 100 vol %, respectively) for 15 minutes in each and finally dried by supercritical CO_2. The resulting aerogel microspheres were pyrolyzed under Ar flow (200 mL/min), increasing the temperature at a rate of 2 ^{o}C/min up to 200 ^{o}C for 2 h and then to 900 ^{o}C for 2 h.

Preparation of sample 12. Briefly, to obtain 10 wt % Co and 5 % Fe in the final Co-Fe@SiO_2 catalyst, the required amount of $Co(OAc)_2$ and $Fe(OAc)_2$ aqueous solution was impregnated to SiO_2 ((Davisil Grade 646), 35-60 mesh, pore size 150 Å) support. After impregnation, the sample was dried at 120 ^{o}C for 12 h, followed by calcination in air at a heating rate of 2 ^{o}C min^{-1} at 400 ^{o}C for 4 h. Then, the material prepared was reduced by H_2 with a heating rate of 5 ^{o}C min^{-1} at 600 ^{o}C for 2 h.

Sample characterization. Field Emission scanning electron microscopy (FESEM) images were acquired by using a JEOL JSM 6300 apparatus. HRTEM images were recorded in a JEOL JEM 2100F under an accelerating voltage of 200 kV. Samples were prepared by applying one drop of the suspended material in ethanol onto a carbon-coated nickel TEM grid and allowing them to dry at room temperature. Raman spectra were collected with a Horiba Jobin Yvon-Labram HR UV-visible-NIR (200-1600 nm) Raman Microscope Spectrometer using a 512 nm laser. The C and N content of the samples was determined by combustion chemical analysis by using a CHNS

FISONS elemental analyser and by ICP-OES analysis of the metals after digesting the samples in *aqua regia*. ICP-OES analysis showed that the Na content of the samples was below 0.1 wt.%.

Catalytic tests. Catalytic tests were performed in a setup (Microactivity Reference, PID Eng&Tech) equipped with a stainless steel (316 SS) fixed bed tube reactor (Autoclave Engineers) featured with an inner K-type thermocouple. Two mass flow controllers (EL-FLOW Select, Bronkhorst) were used to feed the mixture of the inlet gases: H_2 (5.0, Linde) and CO_2 (4.5, Linde). The total gas flow rate was checked before each experiment by help of a gas burette connected to the outlet of the reactor setup.

An amount of 40 mg catalyst powder was introduced in the reactor; air was removed by flushing the system at room temperature for 15 min with 30 mL/min H_2 and 10 mL/min CO_2, followed by 10 min at the flow rates used during the experiments: 3 mL/min H_2 and 1 mL/min CO_2. Afterwards, the reactor was pressurized at 10 bar. Five reaction temperatures between 300 and 500 ^oC were investigated. For each temperature, a set of three successive GC analyses were performed (at 30, 45 and 55 min after the stabilization of the temperature). The values of the CO_2 conversion obtained from the last two GC measurement coincide very well, indicating that the reactor setup reached the steady state operation conditions.

GC analyses were performed using H_2 as carrier gas on an Agilent 7890A chromatograph equipped with a capillary PLOT column (RT-Molsieve 5A, Restek) and a TCD detector. Temperature program includes a 5 min dwell at 50 ^oC, a ramp with 25 ^oC/min to 250 ^oC followed by a final dwell of 5 min, allowing thus a very good separation between O_2, N_2, CH_4, CO and CO_2. The system allows also detection of light hydrocarbons up to C5, but they were below the detection limit. Quantification of these products was performed using as standards certified commercial gas mixtures and calibration plots. The gas samples were injected through a remotely controlled 6-way

valve (A4C6WE, Vici) kept at ambient temperature. The reproducibility of the analytical procedure was checked prior to each experiment by injecting a series of three successive samples of gas mixture passed through the reactor at room temperature.

RESULTS AND DISCUSSION

The catalysts under study were prepared by impregnation of millimetric hydrogel chitosan beads with $Co(OAc)_2$, $Fe(OAc)_2$ or appropriate $Co(OAc)_2$ and $Fe(OAc)_2$ mixtures dissolved in 1:1 water-ethanol, followed by supercritical CO_2 drying of the beads and subsequent pyrolysis. Scheme 1 illustrates the preparation procedure and contains the relevant experimental conditions.

The process starts with the precipitation as microspheres of chitosan dissolved in acidic aqueous solution by neutralization with NaOH. One property of chitosan and related polysaccharides is their ability to adsorb metal salts from aqueous solution.[33] We have taken advantage of this adsorption capacity to co-incorporate Fe and Co salts on chitosan. The resulting hydrogels containing Fe or Co salts or their mixtures were converted to alcogels by dispersing consecutively the beads in three ethanol: water solutions of increased ethanol content up to absolute ethanol. The alcogel microspheres were finally dried in supercritical CO_2. It is well documented in the literature that this procedure renders highly porous chitosan aerogels with a large surface area.[34, 35] Subsequent pyrolysis of chitosan beads have been reported to form graphitic carbon residues that can be exfoliated by sonication into the defective N-doped graphene.[36, 37] It is worth noting that chitosan as a glucosamine polymer is simultaneously the source of C and N, resulting in the pyrolysis of N-doped defective graphene with a N-content about 5 wt.%. According to XPS analyses (see Figure S1), the two main types of N atoms present in (N)G are pyridinic (binding

energy 398.2 eV, sp^2 N atoms at the periphery bonded to two C atoms and giving one electron to the π cloud) and graphitic (binding energy 400.7 eV, sp^2 N atoms bonded to three C atoms and giving one electron to the π cloud) in a proportion about 47:53.[37, 38] If the chitosan beads contain adsorbed transition metals, they are typically converted into metal NPs during the pyrolysis due to the reductive conditions of the process. The term carbochemical reduction has been previously coined to denote the formation of metal NPs or metal alloy NPs upon heating their salts at high temperature in the presence of materials generating carbon residues.[39, 40]

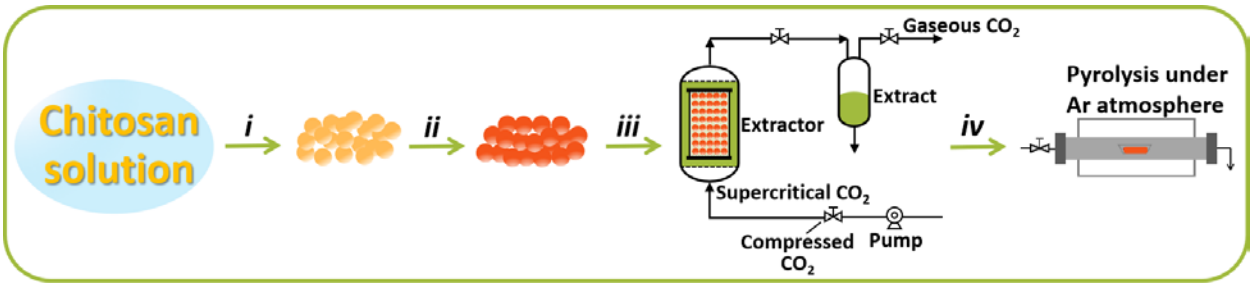

Scheme 1. Simplified procedure used to prepare the Co-Fe@(N)G samples under study. (i) formation of chitosan spheres; (ii) impregnation with $Co(OAc)_2$ and $Fe(OAc)_2$ salts; (iii) supercritical CO_2 drying; (iv) pyrolysis.

Three Co-Fe alloy samples with increasing Co content were prepared. The total metal content of these three samples is low, below 0.2 wt.%. To determine the role of metal loading and particle size on the performance of the catalyst, three more Co-Fe alloy samples were obtained following an identical procedure, but using a higher salt concentration in the range of about 10 wt.%. Single Fe or Co metals supported on (N)G were also synthesized for comparison. The set of catalysts includes an additional sample using SiO_2 as support. Table 1 lists the codes and relevant analytical data of the samples under study.

Table 1. List of samples under study and their main analytical and physicochemical parameters.

Sample No.	Co (wt.%)[a]	Fe (wt.%)[a]	Fe/Co ratio	Total Co+Fe content (wt.%)[a]	Average particle size (nm)[b,c]
1	0.042	0.053	1.26	0.095	<1 nm (CLs)
2	0.081	0.052	0.64	0.133	<1 nm (CLs)
3	0.120	0.053	0.44	0.173	<1 nm (CLs)
4	0.049	-	-	0.049	<1 nm (CLs)
5	-	0.054	-	0.054	<1 nm (CLs)
6	5.21	10.32	1.98	15.53	4.8±0.7 (NPs)
7	5.07	6.65	1.31	11.72	3.8±0.7 (NPs)
8	4.09	2.55	0.62	6.64	2.6±0.7 (NPs)
9	6.10	-	-	6.10	1.0±0.3 (NPs)
10	-	7.89	-	7.89	1.4±0.3 (NPs)
11[d]	11.38	3.92	0.34	15.30	-
12[e]	9.97	4.79	0.48	14.76	-

[a] Determined by ICP-AES analysis after dissolving the metals in aqua regia; [b] Determined by DF-TEM; [c] CLs and NPs refer to clusters and nanoparticles, respectively; [d] Graphitic carbon from alginic acid as support; [e] SiO_2 as support.

The metal content was determined by ICP-AES elemental analysis after dissolving the metals in aqua regia. Co and Fe content values are summarized in Table 1. As it is shown, elemental analysis for samples **1**-**3** showed similar Fe content, but increasing Co loadings, agreeing with the preparation procedure of these samples in which higher amounts of Co were added from samples **1** to **3**. The total Co-Fe content of these three samples **1**-**3** was very low, varying from about 0.10 to 0.17 wt.%. Two additional samples having only either Co (sample **4**) or Fe (sample **5**) at low loadings were also prepared. As expected, in view of the higher salt concentrations used, the Co and Fe content in samples **6** to **8** were about two orders of magnitude higher than for samples **1**-**5** and in the same range as those of single Co or Fe metal (samples **9** and **10**), the sample using undoped graphitic carbon **11** or that of the control sample **12** in which the Co-Fe alloy NPs were supported on SiO_2.

The elemental composition and chemical environments of the Co-Fe@(N)G, Co@(N)G and Fe@(N)G are examined by X-ray photoelectron spectroscopy (XPS). Figures 1a and b exhibit the Co 2p and Fe 2p specta of sample **1**. The high-resolution XPS spectrum of Co $2p_{3/2}$ in Figure 1a exhibits the distinct peaks at 778.3, 780.5 and 786.6 eV, ascribable to zero-valence cobalt, the oxidation state of Co (II), and the satellite peak, respectively. In accordance, the peak corresponding to Co $2p_{1/2}$ can also be deconvoluted with three components, corresponding to metallic Co, Co^{2+} and the satellite peak, respectively. Analogously, the deconvolution of the Fe 2p peak in Figure 1b shows the peaks corresponding to metallic Fe (707.4 eV for Fe $2p_{3/2}$ and 721.0 eV for Fe $2p_{1/2}$), Fe^{2+} (709.2 eV for Fe $2p_{3/2}$ and 722.8 eV for Fe $2p_{1/2}$), Fe^{3+} (710.9 eV for Fe $2p_{3/2}$ and 724.5 eV for Fe $2p_{1/2}$) and satellite peaks (714.5 eV for Fe $2p_{3/2}$ and 728.1 eV for Fe $2p_{1/2}$). The ratio of metallic Co to Co species in sample **1** was of about 46.7 % and the ratio value of metallic Fe to total Fe was even less as 26.4 %. This could be attributed to the high susceptibility of the small Co-Fe clusters to air and surface oxidization, making the surface metallic atoms mainly exist in the form of the high valent states, and the low permeability of the X-ray, making the zero valent Co and Fe in the bulk of Co-Fe clusters less detectable by XPS. The Fe/Co atomic ratio for sample **1** according to XPS is 1.3 that is in good accordance with the value determined by ICP-OES analysis. Similarly, the high-resolution XPS Co $2p_{3/2}$ spectrum of sample **4** in Figure 1c exhibits the distinct peaks at 778.3, 780.5 and 786.5 eV, ascribable to metallic Co, Co^{2+} and the satellite peak, respectively. The high-resolution XPS Fe $2p_{3/2}$ spectrum of sample **5** in Figure 1d exhibits the distinct peaks at 707.0, 709.3, 711.8 and 713.46 eV, corresponding to metallic Fe, the oxidation state of Fe (II), Fe (III) and the satellite peak, respectively. The ratios of zero-valence metal to metal species in samples **4** and **5** were 43.8 % and 25.3 %, respectively.

Figure S1 shows the high-resolution XPS C1s, O1s and N1s spectra of samples **1**, **4** and **5**. The high-resolution XPS C1s peak for all of the samples was conveniently deconvoluted in the four individual components appearing at 284.5, 285.4, 286.4, and 288.7 eV, attributable to graphitic C atoms, C atoms bonded to O or N with single or double bonds, and C atoms of carboxylic groups, respectively. Figures S1a-c shows a representative XPS C1s peak with the best fitting to its individual components, while Table S2 in the Supporting Information lists the percentages of each type of carbon atom. XPS analysis also revealed the presence of O and N in Co-Fe@(N)G, Co@(N)G and Fe@(N)G in similar atomic percentage vs C of about 5 wt. % N doping was in agreement with the thermal behavior of chitosan that formed N-doped graphene. The high-resolution XPS O1s peak was also appropriately deconvoluted into four main components, appearing at 530.5, 531.9, 533.1 and 534.2 eV, attributable to O atoms in metal oxide, C=O, C-O and O-C=O, respectively. Of note is that the good fit between the experimental and deconvoluted O 1s peak indicates that O atoms in metal oxides should be present in very low proportions. Figures S1g-i illustrates the distribution of high-resolution XPS N1s peak into the two major components (pyridinic N and graphitic N) and different N families are in similar proportions for all of the samples, while Table S2 in the Supporting Information lists the percentages of each type of O and N atoms.

The amount of Fe and Co of samples **1-5** was too low and their dispersion too high to detect peaks of these metals in powder X-ray diffraction (XRD, see Figure 1e). In contrast, samples **6** to **12** exhibit in XRD the patterns characteristic of fcc phase for Co and Fe, accompanied by some bcc phase, confirming the presence of metallic Fe-Co NPs and occurrence of carbochemical reduction during the pyrolysis. For samples **6-8**, **11** and **12** containing mixtures of Fe and Co, the minor

variations in the position of the diffraction peak at $2\theta \approx 44^{o}$ suggest that the metal NPs are real Co-Fe alloys, rather than independent Fe and Co NPs, although the very similar cell parameters of Co and Fe make this conclusion somewhat uncertain. Figure 1e presents the XRD spectrum of samples **6-8**, **11** and **12** having bcc cubic phase, where the peaks appear at 44.9^{o} (110) and 65.5^{o} (200) assigned to Co-Fe alloy in comparison with that of Co fcc cubic (Fm3m) structure recorded for sample **9** showing characteristic diffraction peaks at $2\theta = 44.3^{o}$ (111), 51.6^{o} (200) and 75.9^{o} (220). In any case, XRD data for samples **6** to **12** conclusively rules out the presence of detectable amount of metal oxides or the formation in the pyrolysis of the detectable amounts of metal carbides.

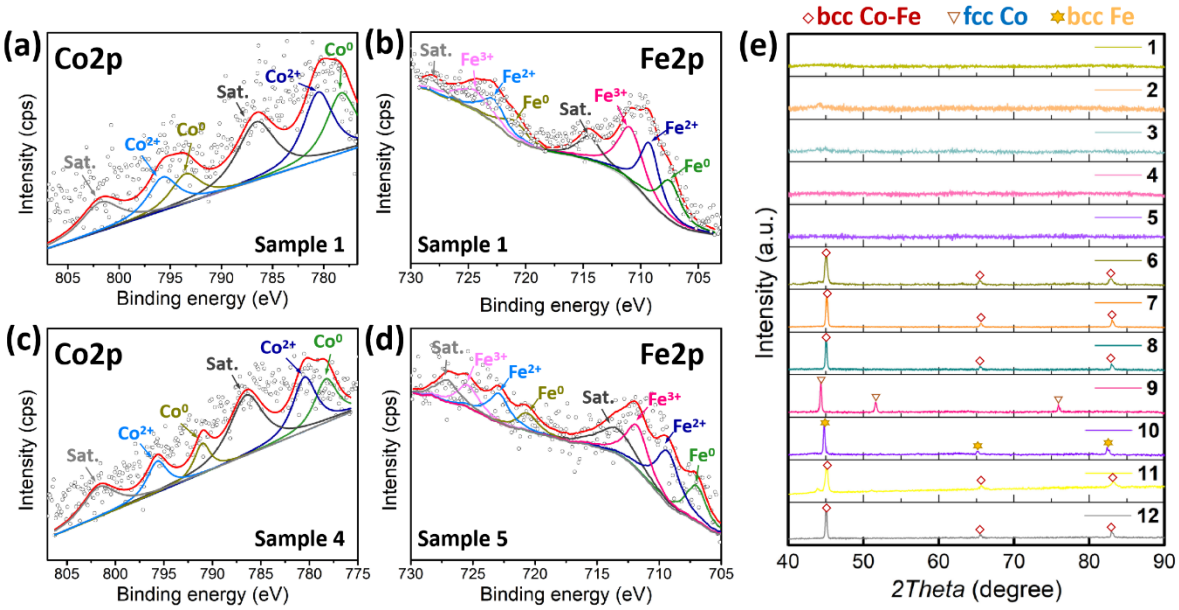

Figure 1. High-resolution Co 2p spectra of sample **1** (a) and sample **4** (c), high-resolution Fe 2p spectra of sample **1** (b) and sample **4** (d) and XRD patterns of the samples **1-12** (e).

In accordance to the literature, the occurrence of the graphitization during the pyrolysis at 900 ºC of chitosan beads (step iv in Scheme 1) was assessed by Raman spectroscopy.[37] As an example to illustrate this point, Figure 2 includes the Raman spectrum recorded for sample **1**, while supporting information (Figure S.2) compiles those for the other samples under study. As shown in Figure 2, the characteristic vibration bands expected for defective graphenes appear in the Raman spectra. The bands at 2960, 2700, 1580 and 1350 cm^{-1} can be assigned to the D+D', 2D, G and D, respectively. In particular, the relative intensity of the G to the D peak of 1.1 is among the expected values for defective graphene.[37] The presence of N and C in the graphitic residues of samples **1** to **10** was determined by combustion chemical analyses, giving a consistent value between 4 and 6 wt.% of N. Supporting information (Table S.1) summarizes the main analytical data of the samples under study.

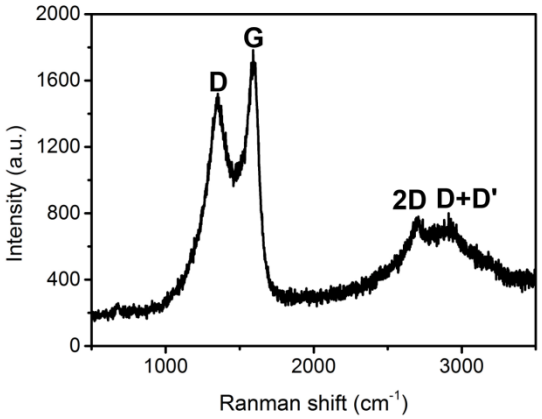

Figure 2. Raman spectroscopy of sample **1**.

Field emission scanning electron microscopy (FESEM) shows that at the micrometer scale samples **1** to **10** are constituted by highly porous, fluffy, cotton-like fibrils. This morphology is inherited from the chitosan aerogel precursor that is also highly porous, cotton-like beads

constituted by the agglomeration of chitosan fibrils. Images corresponding to the samples under study are provided in the supporting information (Figure S.3).

Transmission electron microscopy (TEM) images of the samples reveal clear differences depending on the total metal content. These differences will be highly relevant to rationalize the catalytic activity of the samples. Thus, dark-field (DF) TEM images for samples **1-5** reveal the presence of well dispersed metal as a cloud throughout the carbon matrix without observation in any part of the samples of dots of measurable dimensions that would correspond to small NPs. These images indicate that, at the nanometer resolution of the TEM instrument, samples **1** to **5** are constituted by clusters and that metal NPs of size above 1 nm are absent in these samples (indicated in Table 1 as CL). Figure 3 presents representative DF-TEM images illustrating metal dispersion throughout the carbon matrix. As it can be seen, the images show a bright contrast revealing the location of Co-Fe in the field, but absence of NPs at the 1-2 nm resolution of the TEM instrument. In the literature, there is ample number of precedents showing similar features that are attributed to corresponding to metal CLs.[41, 42] Figure 3 also presents energy dispersive spectrometer (EDS) mappings of sample **1** at micrometer scale. No bright dots corresponding to small NPs could be detected in any part of sample **1** and EDS mappings of Figure 3l display that the Co-Fe species are highly dispersed. However, due to the low loading, no accurate Fe/Co atomic ratio could not be determined by EDS analysis since the signal was barely at the detection limit. Figure S4 presents EDS mappings of samples **4** and **5** at micrometer scale which prove Co and Fe species are highly dispersed in samples **4** and **5** as well.

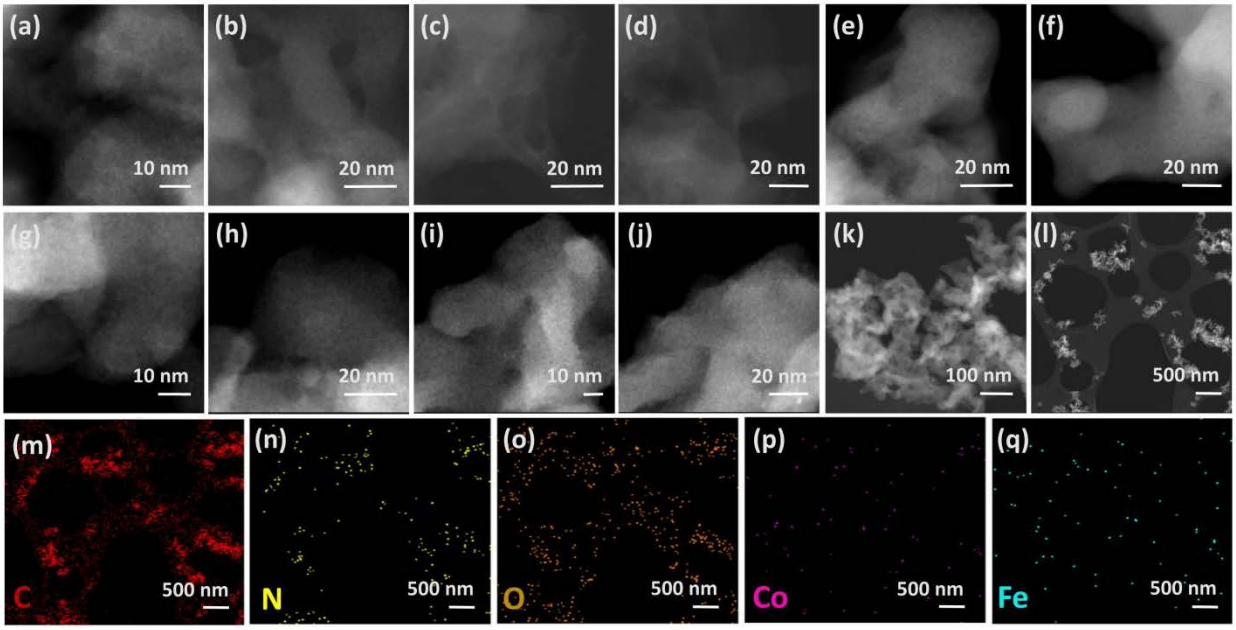

Figure 3. DF-TEM images of samples **1-5** and energy dispersive spectrometric mappings of samples **1** at micrometer scale. (a, b, k, l, m-q: sample **1**; c, d: sample **2**; e, f: sample **3**; g, h: sample **4**; i, j: sample **5**).

In contrast to the case of samples **1-5**, Figure 4 shows selected DF-TEM images corresponding to samples **6** to **8** and the TEM images corresponding to samples **9** and **10** are presented in Figure S.5 of supporting information. DF-TEM images of samples **6-10** clearly shows bright dots due to small metal NPs can be clearly distinguished. The particle size distribution was determined by measuring a statistically relevant number of these NPs. Figure 4 also includes the corresponding histograms from which the average particle sizes indicated in Table 1 was determined. It should be, however, commented that the average particle size determined by these measurements probably overestimates the average size, since these histograms cannot take into account the presence of an undefined number of CLs without measurable dimensions. In any case, it is clear that the particle sizes of samples **6** to **10** are very small in the range from 1 to 5 nm. This small particle size is a remarkable fact, considering that the Co and Fe salts were submitted in the pyrolysis step to 900

^{o}C for hours and the well-known effect of the temperature on increasing the size of the metal particles by aggregation.[43] In this regard, it is proposed that the good dispersion of the Co and Fe salts on the highly porous chitosan precursor and the interaction of the metal particles with the defective N-doped graphene support should be the main reasons responsible for these small particle sizes. The difference in particle size between samples **1** to **5** on one hand, and samples **6** to **10** on the other one, is reasonable considering the previously commented remarkably higher total metal loading of samples **6**-**10** compared to samples **1**-**5**. A careful inspection of DF-TEM images for samples **6**-**10** shows that in contrast to samples **1**-**5**, the brightness indicating the presence of metal is concentrated preferentially in some areas, suggesting that the metals are inhomogeneously distributed on the graphene support (compare images of Figures 3 and 4). For samples **6**-**10**, the Co-Fe metals are mainly located at the ridges and borders of the graphene sheets.

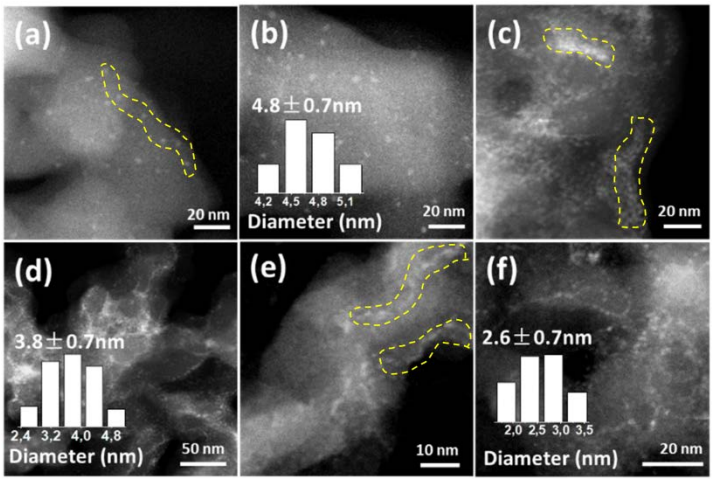

Figure 4. DF-TEM images of samples **6**-**8**. (a, b: sample **6**; c, d: sample **7**; e, f: sample **8**; Inset: the statistical particle size distributions of samples **6**-**8**, respectively.) The yellow dashed lines marked locations in where Co-Fe NPs are present.

The difference in particle size between samples **1**-**5** and **6**-**10** having CLs or NPs is crucial to rationalize their distinctive activity and selectivity for CO_2 hydrogenation that would be much higher for the clusters (samples **1**-**5**) compared to nanoparticles (samples **6**-**10**). Reactions were carried out in pressurized stainless steel tubular reactors at 10 bar under a H_2/CO_2 molar ratio of 7, by heating the system at temperatures from 300 to 450 ^oC in 50 ^oC steps. Each temperature was maintained for 1 h and the reaction products were analyzed at 30, 45 and 59 min after the temperature was set. The complete time of the experiment was 5 h. Preliminary control experiments showed that in the absence of any catalyst or in the presence of (N)G, CO_2 conversion at 450 ^oC under the reaction conditions was 1.9 and 6.0 %, respectively, with complete selectivity to CH_4.

As expected, as a general trend, CO_2 conversion increased for all the catalysts with the temperature, and product selectivity changed with temperature and conversion, making comparison of selectivity for different catalysts at different conversions meaningless. Nevertheless, remarkable differences in activity and selectivity were observed for samples **1**-**5** respect to **6**-**10**. For the CL series (samples **1**-**5**), sample **2** with intermediate Fe/Co ratio perform worst, while for the NP series (samples **6**-**10**) CO_2 conversion increased with the decrease in Fe/Co ratio. This different trend could indicate specific arrangements of Fe and Co atoms in CLs or NPs or at the interface with N-doped graphene. Although modelling and theoretical calculations are needed to gain further understanding on how the Fe/Co ratio determines activity, the results clearly show that for the same catalyst mass (40 mg sample, no binder employed), samples having CLs were far more active and remarkably selective towards RWGS than those having NPs. To illustrate the different catalytic performance, Figure 5a shows conversion and selectivity for these eight samples at 450 ^oC, under the same conditions. As it can be seen there, in spite of the two orders of

magnitude lower metal content of samples **1-5**, the samples with CLs were at least two-fold more active than those containing NPs. This higher activity of samples **1-5** with minute Co and Fe loadings is a reflection of the notable influence of the particle size on the performance that is more important than the influence of Co-Fe alloying.

Besides differences in conversion, CO was the predominant product in all the samples **1-12**. To further optimize the conditions, the performance of samples **1-5** was studied at different temperatures from 300 to 500 ^{o}C in 50 ^{o}C steps (Figure 5b-d and Figure S.6, see supporting information). Sample **1** was the best performing catalyst reaching a conversion at 500 ^{o}C of 56 % with 98 % CO selectivity at a space velocity of 600 h^{-1} (Figure 5b). It should be noted that CO_2 conversion increases as the space velocity decreases and, thus, even higher conversions over 60 % without selectivity change were obtained by using higher amounts (60 mg) of sample **1**. Furthermore, sample **1** was remarkably stable, as confirmed by performing a 30 h run experiment at 450 ^{o}C, observing constant conversion and selectivity. However, DF-TEM characterization of the used sample **1** showed in TEM the appearance of metal NPs (Figure S.7b, see supporting information), indicating that some CL agglomeration and particle growth is taking place under these conditions. This CL agglomeration should be minor since it is not reflected in the catalytic activity of sample **1** in the 30 h run, although it could be the cause of longer term deactivation.

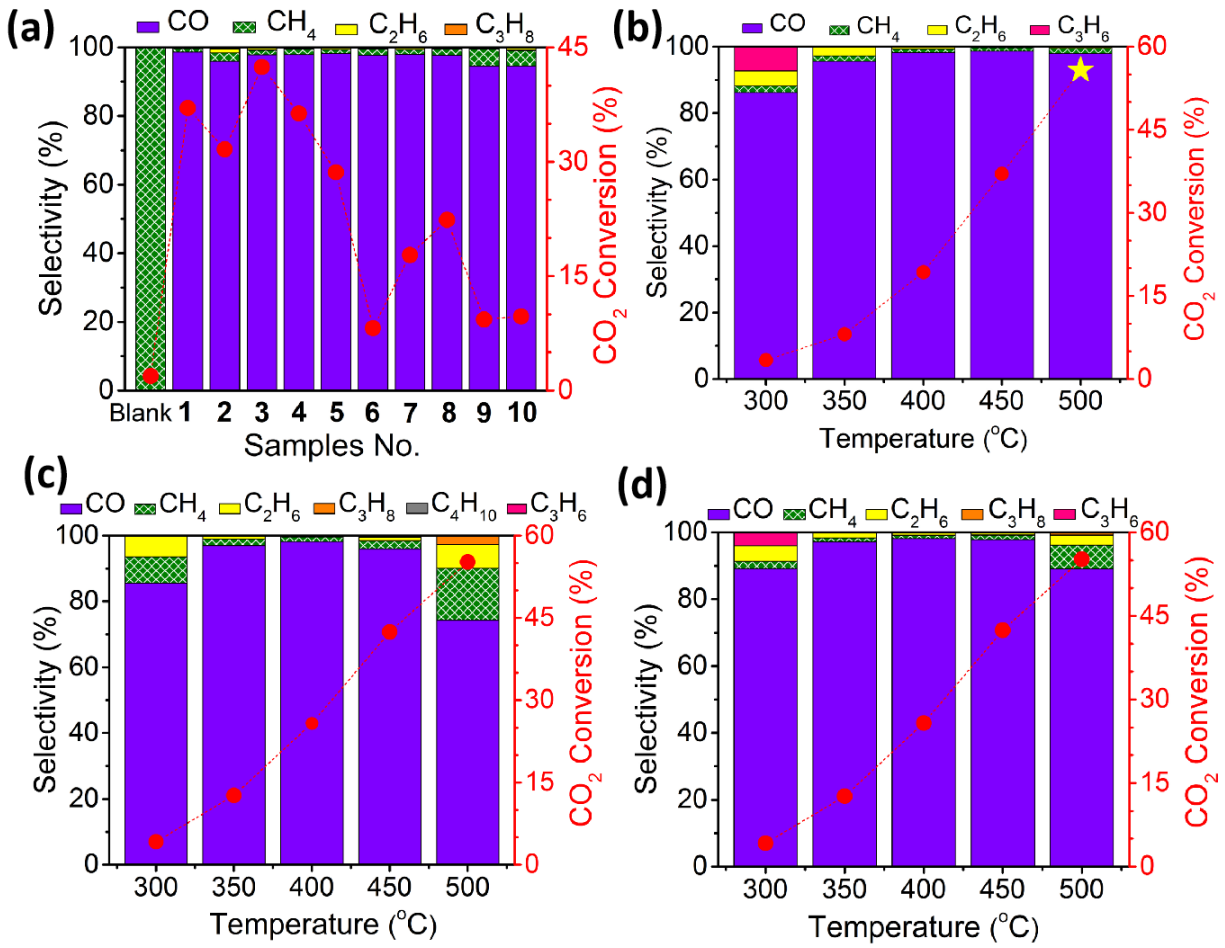

Figure 5. CO_2 conversion and selectivity of samples **1-10** at 450 ºC (a), sample **1** (b), sample **2** (c) and sample **3** (d) at temperatures from 300 to 500 ºC. Reaction conditions: H_2/CO_2 molar ratio of 7, total flow: 4 mL/min; pressure: 10 bar; catalyst amount: 40 mg; space velocity: 600 h^{-1}.

The influence of alloying increasing the activity can be inferred from the comparison of the performance of samples **4** and **5** or **9** and **10**, having only Co or Fe, with those of samples **1-3** and **6-8**, respectively (Figure 5a). At 450 ºC, the activity of sample **4** (only Co, 36 % CO_2 conversion) was better than that of sample **5** (only Fe, 29 % CO_2 conversion) and both of them were less active that samples **1** (37 % CO_2 conversion) and **3** (42 % CO_2 conversion). Worth nothing is that higher

activity, even in a few percents, may represent a large competitive advantage in large scale reactions. This influence of alloy is also observed for NPs in which the performance of samples **9** and **10** is worst in spite that their particle size is are notably smaller. It seems that in the range of atomic ratio studied, the increase of the Co proportion results in an increase of the catalytic activity. In addition, alloying also increases significantly the selectivity towards RWGS. Thus, for both types of catalysts, CLs and NPs there are alloyed samples surpassing in activity those of the single metal. Supporting information (Figure S.8) provides the performance of samples **6-10** at different temperatures.

The role of (N)G as support was finally addressed by preparing an alternative Fe-Co NPs supported on SiO_2. Catalysts based on Co supported on silica are standard catalysts for CO_2 hydrogenation.[44] The activity data for sample **12** is given in Figure S.9 of supporting information. Although, Co-Fe NPs supported on SiO_2 exhibit a comparable activity for CO_2 hydrogenation in terms of CO_2 conversion, the main product for sample **12** with SiO_2 as support was consistently methane over 50 % selectivity in all the range of temperatures from 300 to 450 ^{o}C. Even the presence of minor amounts of ethane (4.8 %) and propane (0.5 %) could be detected at 450 ^{o}C. These contrasting selectivity for Fe-Co alloys supported on (N)G or SiO_2 illustrates once again the large influence that the support plays on the catalyst performance and product selectivity of active centers. This influence of the support derives from the delicate balance among charge transfer from the support to the Fe-Co sites, adsorption of reaction intermediates and surface acidity, among other properties of the support.

CONCLUSIONS

The present study has shown the remarkable performance of Co-Fe clusters of (sub)nanometer-size supported on defective N-doped graphitic carbon compared to analogous metal NPs of size ranging from 1 to 5 nm on the same support. A minute amount below 0.2 wt.% of highly dispersed Co-Fe clusters is sufficient to achieve optimal catalytic activity with a remarkable RWGS selectivity and high catalytic stability. It seems, however, that cluster agglomeration into nanoparticles could eventually decrease activity and product selectivity at times longer than the 30 h run tested. The present results draw the attention of the influence in the CO_2 hydrogenation of the particle size on the nanometer regime and the nature of the support on the activity and selectivity of Co-Fe catalyst, something that is known in Fisher-Tropsch synthesis, but it is much less documented for CO_2.

AUTHOR INFORMATION

Corresponding Authors

Prof. Hermenegildo García: hgarcia@qim.upv.es;

Prof. Vasile I. Parvulescu: vasile.parvulescu@chimie.unibuc.ro

Author Contributions

L.P prepared and characterize the samples; B.J. perform the catalytic experiments; A.P. and A.G supervised the work; the concept of the study was designed by V.P. and H.G. The manuscript was written through contributions of all authors. All authors have given approval to the final version of the manuscript. ‡These authors contributed equally.

ACKNOWLEDGMENTS

Financial support by the Spanish Ministry of Science, Innovation and University (Severo Ochoa and RTI2018.98237-B-CO1) and Generalitat Valenciana (Prometeo 2017/083) is gratefully acknowledged. L.P. thanks the Generalitat Valenciana for a Santiago Grisolía scholarship. BASF is thanked for financial support.

SUPPORTING INFORMATION

Table with the amounts of reagents used for sample preparation. Figures with high-resolution XPS C, O, N peaks, Raman spectra, FESEM images, Reactivity data of the samples and comparison of the TEM images of the fresh and used sample **1**.

REFERENCES

1. Anderson, T. R.; Hawkins, E.; Jones, P. D. CO_2, the greenhouse effect and global warming: from the pioneering work of Arrhenius and Callendar to today's Earth System Models, *Endeavour* **2016,** *40*, 178-187. (DOI: 10.1016/j.endeavour.2016.07.002)
2. Matthews, H. D.; Caldeira, K. Stabilizing climate requires near-zero emissions, *Geophysical research letters* **2008,** *35*. (DOI: 10.1029/2007GL032388)
3. Molina, M.; Zaelke, D.; Sarma, K. M.; Andersen, S. O.; Ramanathan, V.; Kaniaru, D. Reducing abrupt climate change risk using the Montreal Protocol and other regulatory actions to complement cuts in CO_2 emissions, *Proceedings of the National Academy of Sciences* **2009,** *106*, 20616-20621. (DOI: 10.1073/pnas.0902568106)
4. Al-Mamoori, A.; Krishnamurthy, A.; Rownaghi, A. A.; Rezaei, F. Carbon capture and utilization update, *Energy Technology* **2017,** *5*, 834-849. (DOI: 10.1002/ente.201600747)
5. Stuardi, F. M.; MacPherson, F.; Leclaire, J. Integrated CO_2 capture and utilization: A priority research direction, *Current Opinion in Green and Sustainable Chemistry* **2019,** *16*, 71-76. (DOI: 10.1016/j.cogsc.2016.07.002)

6. Yu, K. M. K.; Curcic, I.; Gabriel, J.; Tsang, S. C. E. Recent advances in CO_2 capture and utilization, *ChemSusChem: Chemistry & Sustainability Energy & Materials* **2008,** *1*, 893-899. (DOI: 10.1002/cssc.200800169)
7. Frontera, P.; Macario, A.; Ferraro, M.; Antonucci, P. Supported catalysts for CO_2 methanation: a review, *Catalysts* **2017,** *7*, 59. (DOI: 10.3390/catal7020059)
8. Fujita, S.-I.; Takezawa, N. Difference in the selectivity of CO and CO_2 methanation reactions, *Chemical Engineering Journal* **1997,** *68*, 63-68. (DOI: 10.1016/S1385-8947(97)00074-0)
9. Kattel, S.; Ramírez, P. J.; Chen, J. G.; Rodriguez, J. A.; Liu, P. Active sites for CO_2 hydrogenation to methanol on Cu/ZnO catalysts, *Science* **2017,** *355*, 1296-1299. (DOI: 10.1126/science.aal3573)
10. Pastor-Pérez, L.; Baibars, F.; Le Sache, E.; Arellano-García, H.; Gu, S.; Reina, T. R. CO_2 valorisation via reverse water-gas shift reaction using advanced Cs doped Fe-Cu/Al_2O_3 catalysts, *Journal of CO_2 Utilization* **2017,** *21*, 423-428. (DOI: 10.1016/j.jcou.2017.08.009)
11. Weatherbee, G. D.; Bartholomew, C. H. Hydrogenation of CO_2 on group VIII metals: II. Kinetics and mechanism of CO_2 hydrogenation on nickel, *Journal of Catalysis* **1982,** *77*, 460-472. (DOI: 10.1016/0021-9517(82)90186-5)
12. Byron, R., . Smith; Loganathan, M.; Shantha, M. S. A review of the water gas shift reaction kinetics, *International Journal of Chemical Reactor Engineering* **2010,** *8*. (DOI: 10.2202/1542-6580.2238)
13. Chen, C.-S.; Cheng, W.-H.; Lin, S.-S. Study of reverse water gas shift reaction by TPD, TPR and CO_2 hydrogenation over potassium-promoted Cu/SiO_2 catalyst, *Applied Catalysis A: General* **2003,** *238*, 55-67. (DOI: 10.1016/S0926-860X(02)00221-1)
14. Chen, C.-S.; Cheng, W.-H.; Lin, S.-S. Study of iron-promoted Cu/SiO_2 catalyst on high temperature reverse water gas shift reaction, *Applied Catalysis A: General* **2004,** *257*, 97-106. (DOI: 10.1016/S0926-860X(03)00637-9)
15. Ginés, M.; Marchi, A.; Apesteguia, C. Kinetic study of the reverse water-gas shift reaction over CuO/ZnO/Al_2O_3 catalysts, *Applied Catalysis A: General* **1997,** *154*, 155-171. (DOI: 10.1016/S0926-860X(96)00369-9)
16. Daza, Y. A.; Kuhn, J. N. CO_2 conversion by reverse water gas shift catalysis: comparison of catalysts, mechanisms and their consequences for CO_2 conversion to liquid fuels, *RSC advances* **2016,** *6*, 49675-49691. (DOI: 10.1039/C6RA05414E)
17. Anderson, R. B.; Kölbel, H.; Rálek, M. *The fischer-tropsch synthesis*. Academic Press New York: 1984; Vol. 16.
18. Dry, M. E.,The fischer-tropsch process: 1950-2000, *Catalysis today* **2002,** *71*, 227-241. (DOI: 10.1016/S0920-5861(01)00453-9)
19. Van Der Laan, G. P.; Beenackers, A. Kinetics and selectivity of the Fischer-Tropsch synthesis: a literature review, *Catalysis Reviews* **1999,** *41*, 255-318. (DOI: 10.1081/CR-100101170)
20. Li, W.; Wang, H.; Jiang, X.; Zhu, J.; Liu, Z.; Guo, X.; Song, C. A short review of recent advances in CO_2 hydrogenation to hydrocarbons over heterogeneous catalysts, *RSC advances* **2018,** *8*, 7651-7669. (DOI: 10.1039/C7RA13546G)
21. Wang, W.; Wang, S.; Ma, X.; Gong, J. Recent advances in catalytic hydrogenation of carbon dioxide, *Chemical Society Reviews* **2011,** *40*, 3703-3727. (DOI: 10.1039/C1CS15008A)
22. Ji, D.; Zhou, H.; Tong, Y.; Wang, J.; Zhu, M.; Chen, T.; Yuan, A. Facile fabrication of MOF-derived octahedral CuO wrapped 3D graphene network as binder-free anode for high

performance lithium-ion batteries, *Chemical Engineering Journal* **2017,** *313*, 1623-1632. (DOI: 10.1016/j.cej.2016.11.063)
23. Navalon, S.; Dhakshinamoorthy, A.; Alvaro, M.; Garcia, H. Metal nanoparticles supported on two-dimensional graphenes as heterogeneous catalysts, *Coordination Chemistry Reviews* **2016,** *312*, 99-148. (DOI: 10.1016/j.ccr.2015.12.005)
24. Yang, X.-F.; Wang, A.; Qiao, B.; Li, J.; Liu, J.; Zhang, T. Single-atom catalysts: a new frontier in heterogeneous catalysis, *Accounts of chemical research* **2013,** *46*, 1740-1748. (DOI: 10.1021/ar300361m)
25. Zhou, M.; Zhang, A.; Dai, Z.; Feng, Y. P.; Zhang, C. Strain-enhanced stabilization and catalytic activity of metal nanoclusters on graphene, *The Journal of Physical Chemistry C* **2010,** *114*, 16541-16546. (DOI: 10.1021/jp105368j)
26. Zhang, X.; Lu, Z.; Xu, G.; Wang, T.; Ma, D.; Yang, Z.; Yang, L. Single Pt atom stabilized on nitrogen doped graphene: CO oxidation readily occurs via the tri-molecular Eley-Rideal mechanism, *Physical Chemistry Chemical Physics* **2015,** *17*, 20006-20013. (DOI: 10.1039/C5CP01922B)
27. Fampiou, I.; Ramasubramaniam, A. Binding of Pt nanoclusters to point defects in graphene: adsorption, morphology, and electronic structure, *The Journal of Physical Chemistry C* **2012,** *116*, 6543-6555. (DOI: 10.1021/jp2110117)
28. Okamoto, Y. Density-functional calculations of icosahedral M_{13} (M= Pt and Au) clusters on graphene sheets and flakes, *Chemical physics letters* **2006,** *420*, 382-386. (DOI: 10.1016/j.cplett.2006.01.007)
29. Ouyang, Y.; Li, Q.; Shi, L.; Ling, C.; Wang, J. Molybdenum sulfide clusters immobilized on defective graphene: a stable catalyst for the hydrogen evolution reaction, *Journal of Materials Chemistry A* **2018,** *6*, 2289-2294. (DOI: 10.1039/C7TA09828F)
30. Sen, D.; Thapa, R.; Chattopadhyay, K. Small Pd cluster adsorbed double vacancy defect graphene sheet for hydrogen storage: A first-principles study, *International journal of hydrogen energy* **2013,** *38*, 3041-3049. (DOI: 10.1016/j.ijhydene.2012.12.113)
31. Yang, G.; Fan, X.; Shi, S.; Huang, H.; Zheng, W. Stability of Ptn cluster on free/defective graphene: A first-principles study, *Applied Surface Science* **2017,** *392*, 936-941. (DOI: 10.1016/j.apsusc.2016.09.129)
32. Jurca, B.; Bucur, C.; Primo, A.; Concepción, P.; Parvulescu, V. I.; García, H. N-doped defective graphene from biomass as catalyst for CO_2 hydrogenation to methane, *ChemCatChem* **2019,** *11*, 985-990. (DOI: 10.1002/cctc.201801984)
33. Onsøyen, E.; Skaugrud, O. Metal recovery using chitosan, *Journal of chemical technology and biotechnology (Oxford, Oxfordshire: 1986)* **1990,** *49*, 395-404. (DOI: 10.1002/jctb.280490410)
34. El Kadib, A.; Bousmina, M. Chitosan bio-based organic-inorganic hybrid aerogel microspheres, *Chemistry-A European Journal* **2012,** *18*, 8264-8277. (DOI: 10.1002/chem.201104006)
35. Valentin, R.; Molvinger, K.; Quignard, F.; Brunel, D. Supercritical CO_2 dried chitosan: an efficient intrinsic heterogeneous catalyst in fine chemistry, *New Journal of Chemistry* **2003,** *27*, 1690-1692. (DOI: 10.1039/B310109F)
36. Primo, A.; Atienzar, P.; Sanchez, E.; Delgado, J. M.; García, H. From biomass wastes to large-area, high-quality, N-doped graphene: catalyst-free carbonization of chitosan coatings on arbitrary substrates, *Chemical communications* **2012,** *48*, 9254-9256. (DOI: 10.1039/C2CC34978G)

37. Primo, A.; Sánchez, E.; Delgado, J. M.; García, H. High-yield production of N-doped graphitic platelets by aqueous exfoliation of pyrolyzed chitosan, *Carbon* **2014,** *68*, 777-783. (DOI: 10.1016/j.carbon.2013.11.068)
38. Wei, D.; Liu, Y.; Wang, Y.; Zhang, H.; Huang, L.; Yu, G. Synthesis of N-Doped Graphene by Chemical Vapor Deposition and Its Electrical Properties, *Nano Letters* **2009,** *9*, 1752-1758. (DOI: 10.1021/nl803279t)
39. Abellan, G.; Latorre-Sanchez, M.; Fornes, V.; Ribera, A.; García, H. Graphene as a carbon source effects the nanometallurgy of nickel in Ni, Mn layered double hydroxide-graphene oxide composites, *Chemical Communications* **2012,** *48*, 11416-11418. (DOI: 10.1039/C2CC35750J)
40. Latorre-Sanchez, M.; Atienzar, P.; Abellan, G.; Puche, M.; Fornés, V.; Ribera, A.; García, H. The synthesis of a hybrid graphene-nickel/manganese mixed oxide and its performance in lithium-ion batteries, *Carbon* **2012,** *50*, 518-525. (DOI: 10.1016/j.carbon.2011.09.007)
41. An, S.; Zhang, G.; Wang, T.; Zhang, W.; Li, K.; Song, C.; Miller, J. T.; Miao, S.; Wang, J.; Guo, X. High-Density Ultra-small Clusters and Single-Atom Fe Sites Embedded in Graphitic Carbon Nitride (g-C_3N_4) for Highly Efficient Catalytic Advanced Oxidation Processes, *ACS Nano* **2018,** *12*, 9441-9450. (DOI: 10.1021/acsnano.8b04693)
42. Wang, R.; Yang, J.; Chen, X.; Zhao, Y.; Zhao, W.; Qian, G.; Li, S.; Xiao, Y.; Chen, H.; Ye, Y.; Zhou, G.; Pan, F. Highly Dispersed Cobalt Clusters in Nitrogen-Doped Porous Carbon Enable Multiple Effects for High-Performance Li-S Battery, *Advanced Energy Materials* **2020,** *10*, 1903550. (DOI: 10.1002/aenm.201903550)
43. Sandoval, A.; Gómez-Cortés, A.; Zanella, R.; Díaz, G.; Saniger, J. M. Gold nanoparticles: Support effects for the WGS reaction, *Journal of Molecular Catalysis A: Chemical* **2007,** *278*, 200-208. (DOI: 10.1016/j.molcata.2007.09.014)
44. Garbarino, G.; Cavattoni, T.; Riani, P.; Busca, G. Support effects in metal catalysis: a study of the behavior of unsupported and silica-supported cobalt catalysts in the hydrogenation of CO_2 at atmospheric pressure, *Catalysis Today* **2020,** *345*, 213-219. (DOI: 10.1016/j.cattod.2019.10.016)

For Table of Contents use only

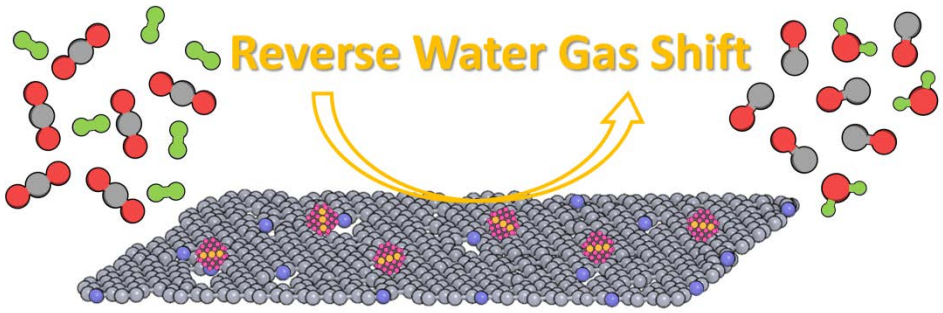

Tiny Co-Fe clusters strongly interacting with a N-doped graphitic carbon matrix are highly active sites for the selective CO_2 hydrogenation to CO.